

Force Field Development from Periodic Density Functional Theory Calculations for Gas Separation Applications Using Metal–Organic Frameworks

Rocio Mercado,[†] Bess Vlaisavljevich,[‡] Li-Chiang Lin,[‡] Kyuho Lee,^{‡,||,⊥} Yongjin Lee,[#] Jarad A. Mason,[†] Dianne J. Xiao,[†] Miguel I. Gonzalez,[†] Matthew T. Kapelewski,[†] Jeffrey B. Neaton,^{||,§} and Berend Smit^{*‡,†,‡,#}

[†]Department of Chemistry, [‡]Department of Chemical and Biomolecular Engineering, and [§]Department of Physics, University of California, Berkeley, Berkeley, California 94720-1462, United States

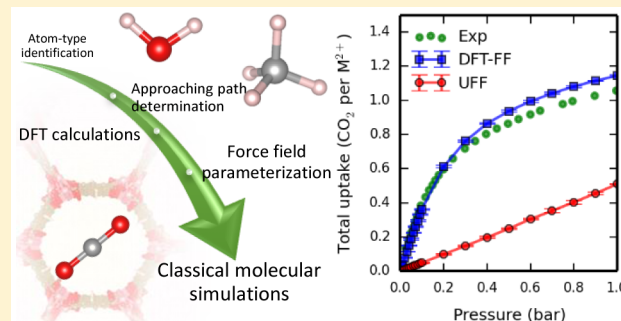
^{||}Molecular Foundry, Lawrence Berkeley National Laboratory, Berkeley, California 94720, United States

[⊥]Synopsys, Inc., Mountain View, California 94043, United States

[#]Institut des Sciences et Ingénierie Chimiques, Valais, École Polytechnique Fédérale de Lausanne (EPFL), Rue de l'Industrie 17, CH-1951 Sion, Switzerland

Supporting Information

ABSTRACT: We present accurate force fields developed from density functional theory (DFT) calculations with periodic boundary conditions for use in molecular simulations involving $M_2(\text{dobdc})$ ($M\text{-MOF-74}$; $\text{dobdc}^{4-} = 2,5\text{-dioxido}1,4\text{-benzenedicarboxylate}$; $M = \text{Mg, Mn, Fe, Co, Ni, Zn}$) and frameworks of similar topology. In these systems, conventional force fields fail to accurately model gas adsorption due to the strongly binding open-metal sites. The DFT-derived force fields predict the adsorption of CO_2 , H_2O , and CH_4 inside these frameworks much more accurately than other common force fields. We show that these force fields can also be used for $M_2(\text{dobpdc})$ ($\text{dobpdc}^{4-} = 4,4'\text{-dioxidobiphenyl-3,3'-dicarboxylate}$), an extended version of MOF-74, and thus are a promising alternative to common force fields for studying materials similar to MOF-74 for carbon capture applications. Furthermore, it is anticipated that the approach can be applied to other metal–organic framework topologies to obtain force fields for different systems. We have used this force field to study the effect of contaminants such as H_2O and N_2 upon these materials' performance for the separation of CO_2 from the emissions of natural gas reservoirs and coal-fired power plants. Specifically, mixture adsorption isotherms calculated with these DFT-derived force fields showed a significant reduction in the uptake of many gas components in the presence of even trace amounts of H_2O vapor. The extent to which the various gases are affected by the concentration of H_2O in the reservoir is quantitatively different for the different frameworks and is related to their heats of adsorption. Additionally, significant increases in CO_2 selectivities over CH_4 and N_2 are observed as the temperature of the systems is lowered.



INTRODUCTION

Efficient separation of gas mixtures plays an important role in various industrial processes, such as the separation of carbon dioxide from coal-gas flues and of methane from natural gas feeds, both of which have significant environmental implications. Because of their large internal surface areas, preferential adsorption of certain gas components over others, and excellent tunability, metal–organic frameworks (MOFs) have been regarded as a promising class of materials for these and other gas separation applications (e.g., carbon capture, separations of hydrocarbon mixtures, noble gas separations). MOFs are nanoporous crystalline materials consisting of organic linkers and inorganic metal sites. These materials are also considered for gas storage applications such as hydrogen and methane storage.^{1–6}

M-MOF-74, also known as $M_2(\text{dobdc})$ and M-CPO-27 in the literature, is a well-known metal–organic framework composed of either magnesium or first-row transition metal nodes ($M = \text{Mg, Mn, Fe, Co, Ni, Cu, or Zn}$) linked by $2,5\text{-dioxido}1,4\text{-benzenedicarboxylate}$ (dobdc^{4-}) linkers to form one-dimensional hexagonal channels lined with coordinatively unsaturated metal sites (Figure S1).⁷ This MOF has a large adsorption capacity and selectivity for CO_2 over many gases.^{1,4,8–11} During the crystallization of such frameworks from solution, solvent molecules directly coordinate to the metal sites. Once the MOF crystals are formed, the material is

Received: April 3, 2016

Revised: May 20, 2016

Published: May 25, 2016

activated by removing these solvent molecules, leaving behind unsaturated metal sites (i.e., so-called open-metal sites). These open-metal sites provide strong binding for guest molecules and bestow the frameworks with remarkable capacities and selectivities for CO₂ over more weakly binding gases like N₂ or CH₄.^{12–16}

Because these open-metal site MOFs are high-performing materials for CO₂/N₂ separations, it is of fundamental interest to accurately describe the interactions of the gases with these open-metal sites. Knowledge of these interactions is of practical importance in molecular simulations. For example, screening huge libraries of both existing and hypothetical materials for CO₂ adsorption using Monte Carlo simulations can accelerate the discovery of materials that are both impervious to contaminants and have large capacities for CO₂ without spending valuable time synthesizing and testing materials that do not possess these qualities. Molecular simulations can be especially valuable when the synthesis of these materials is tricky or time-consuming.^{17–20} One of the challenges with using molecular simulations to accelerate the discovery of new materials is that common force fields, such as the Universal Force Field (UFF)²¹ and the Dreiding force field,²² do not adequately describe the interaction strength between guest adsorbates and the open-metal sites present in many of these high-performing structures, yielding only a poor estimation of their gas adsorption and separation performances in molecular simulations.^{19,23} Motivated by the lack of adequate force fields for studying CO₂ separations in these systems, many groups have focused on developing better models and improving the accuracy of existing models for these systems using ab initio calculations.^{24–27} Similarly, in previous work, we have presented methodologies for developing force fields generalizable to open-metal site structures from only a small number of single-point ab initio calculations using various levels of theory.^{28,29} We found that using DFT calculations with periodic boundary conditions removed any constraints imposed by the use of cluster calculations, and led to force fields that not only correctly predict adsorption isotherms but also binding geometries and transport properties.²⁹ Additionally, most of the first-row MOF-74 frameworks are well studied experimentally, allowing for easy comparison between any new calculations and the assortment of existing data in the literature.

In our previous work, Lin et al.,²⁹ we were limited to studying H₂O and CO₂ adsorption in Mg- and Zn-MOF-74. Here, we extend that work to study H₂O, CO₂, and CH₄ adsorption in six M-MOF-74 (M = Mg, Mn, Fe, Co, Ni, and Zn) frameworks by developing force fields for the series of isostructural MOFs from DFT calculations with periodic boundary conditions. This allows us to obtain systematic insights on how changing the metal center affects the gas adsorption properties in MOF-74.

Although these materials have been widely studied, the performance of MOF-74 in the aforementioned gas separations remains largely unknown; moreover, equilibrium adsorption isotherms for mixtures of gases in MOFs were entirely absent from the literature until recently.³⁰ Given the challenges of measuring adsorption equilibria of gas mixtures, our force fields allow us to carefully study the interaction of gas mixtures with MOFs through the use of molecular simulations. We use our force fields to address the separation of CO₂ from other gases at conditions relevant to natural gas and postcombustion flue gas feeds. Additionally, we show that our force fields can be used to

model adsorption in other frameworks with similar open-metal sites, such as M₂(dobpdc).

METHODOLOGY

Overview. Our force fields were developed to model interactions between CH₄, H₂O, and CO₂ with six M-MOF-74 frameworks (M = Mg, Mn, Fe, Co, Ni, and Zn). Because of the challenge posed by the significant elongation observed in the apical oxygen–metal bond lengths in Cu-MOF-74 (which leads to an elongation of the *c*-axis lattice constants when compared to the other M-MOF-74 structures),¹⁶ we chose not to develop force field parameters for Cu-MOF-74 as that would require significant alterations to our fitting procedure.

First, we describe the types of force fields that were used. In cases where the pairwise nonbonding interactions between framework atoms and guest molecules were fit, we describe the potentials using Buckingham + Coulomb interactions (eq 1), where for each pair of atoms in the system five parameters are specified: A_{ij} , B_{ij} , C_{ij} , q_i , and q_j (the pre-exponential term, exponential term, attractive term, and point charges, respectively). This leads to the following expression for the interaction energy:

$$E_{ij} = \begin{cases} \infty & \text{if } r_{ij} < R_{\min} \\ A_{ij} e^{-B_{ij}r_{ij}} - S_g \frac{C_{ij}}{r_{ij}^6} + \frac{q_i q_j}{4\pi\epsilon_0 r_{ij}} & \text{if } r_{ij} \geq R_{\min} \end{cases} \quad (1)$$

Here, r_{ij} is the distance between atoms i and j , ϵ_0 is the permittivity of free space, R_{\min} is used to prevent the conventional Buckingham potential from going to negative infinity at short distances, and S_g is a scaling factor.

This scaling factor was introduced in the work of Lin et al.²⁹ In the proposed approach (also applied herein), only the repulsive parameters are fit (A_{ij} and B_{ij}). Because the C_{ij} parameters are taken from the literature and the charges are chosen prior to fitting, the “repulsive” portion of the energy may turn out to be negative after the energy decomposition step. Because this implies that the attractive portion of the energy is not large enough, the smallest scaling factor required for the repulsive portion of the energy to be positive at all points is applied to the attractive term in the potential. This choice was tested and found to be reasonable in the previous work.

Interaction parameters were determined for the oxygen atoms in CO₂ interacting with all of the framework atoms except hydrogen. As the oxygen atoms dominate the interaction, we did not further refine the interaction parameters for the carbon in CO₂ with any framework atoms, and instead Lorentz–Berthelot mixing rules were used to determine Lennard-Jones parameters from UFF and EPM2³¹ parameters. Interaction parameters were determined for both the hydrogen and the oxygen atoms in H₂O interacting with all framework atoms except hydrogen and O_a (for more details, please see the Force Field Parameterization section; for atom-type labels, see Figure S1).²⁹ O_a interaction parameters were left out of the parametrization loop to allow for convergence of the remaining interaction parameters. A united atom model was used for CH₄, and interaction parameters were determined for CH₄ interactions with all framework atoms except hydrogen.

For guest–guest nonbonding interactions, as well as the specific nonbonding interactions between the framework and guest atoms mentioned above as exceptions to the fitting

procedure, Lennard-Jones + Coulomb potentials were used (eq 2).

$$E_{ij} = 4\epsilon_{ij} \left[\left(\frac{\sigma_{ij}}{r_{ij}} \right)^{12} - \left(\frac{\sigma_{ij}}{r_{ij}} \right)^6 \right] + \frac{q_i q_j}{4\pi\epsilon_0 r_{ij}} \quad (2)$$

Four parameters were specified for each pair of atoms in the system: ϵ_{ij} , σ_{ij} , q_i , and q_j (the energy parameter, distance parameter, and point charges, respectively). Lorentz–Berthelot mixing rules were employed to determine interactions between different atom-types from the UFF force field and the respective guest models (TraPPE for CH₄,³² EPM2 for CO₂,³¹ and TIP4P-Ew for H₂O).^{33,34} The point charges for the guest atoms were also adopted from the guest models.

In all simulations, frameworks and guest molecules were treated as rigid. More details regarding the fitting will be presented in the [Energy Decomposition](#) and [Force Field Parameterization](#) sections.

Structure Optimization. Geometry optimizations were performed for each framework using density functional theory with periodic boundary conditions as implemented in the Vienna Ab initio Simulation Package (VASP).³⁵ All DFT calculations were performed with PBE³⁶ and vdW-DF2³⁷ functionals, a plane wave basis set, projector augmented wave (PAW) pseudopotentials, and periodic boundary conditions.^{36,38,39} Spin polarized calculations were performed for Fe, Co, and Ni. The starting magnetic moments were chosen on the basis of the high spin state of the +2 oxidation state of each metal (4, 3, and 2 for Fe, Co, and Ni, respectively). The spins were ferromagnetically coupled down the *c*-axis and antiferromagnetically coupled across the *ab*-plane. For transition metals sites with unpaired electrons (Mn, Fe, Co, and Ni), on-site Hubbard *U* corrections were employed with values of 3.8, 4.0, 3.3, and 6.4, respectively. These values have been previously determined to reproduce the oxidation energies of metal oxides.⁴⁰ The cutoff in the plane wave basis was taken to be 1000 eV, and Γ -point sampling was used.

Atom-Types Identification and Approaching Paths Determination. Force fields were fit for three different guests: CH₄, H₂O, and CO₂. In our force fields, each unique atom-type in the guest interacts differently with each unique atom-type in the framework, meaning that each pairwise interaction requires new A_{ij} , B_{ij} , and C_{ij} parameters as well as new point charges q_i and q_j . MOF-74 is composed of four different elements: the metal atom-type, carbon, oxygen, and hydrogen. Considering the local environment of each element in the framework, there are three unique oxygen atom-types (O_a, O_b, O_c), and four unique carbon atom-types (C_a, C_b, C_c, C_d; [Figure S1](#)). All of the metal atoms and hydrogen atoms are in the same local environment in MOF-74.

The first step in our methodology for fitting a given set of pairwise interaction parameters is to determine the approaching path of a given guest molecule toward the target atom-type. This orientation is determined by minimizing the repulsive energy between the guest molecule and other the framework atom-types (i.e., those that are not the target atom). This procedure ensures that the pairwise repulsive interaction between the guest molecule and the target atom dominates the total repulsive energy. The UFF force field and guest force field (along with Lorentz–Berthelot mixing rules) are used to determine these paths. For each path, we use 31 configurations at 0.1 Å intervals apart (from 2.0 to 5.0 Å) to compute the

interaction energy with DFT (as described in the [Methodology](#)).

Interaction Energy Calculation. Once the approaching path has been determined between each pair of atoms, the interaction energies for each configuration along the path are computed using van der Waals corrected DFT and periodic boundary conditions. The interaction energy is defined as the difference in the energy between the MOF and bound guest molecule and their individual energies at infinite separation. Our DFT calculations were performed at the same level of theory as was used for the structure relaxation; however, we found that a dispersion-corrected functional is required to properly describe framework guest interactions. For this reason, following ref 16, single-point calculations to determine total energies were performed for the framework alone with vdW-DF2.³⁷

Energy Decomposition. The interaction energies for these configurations are then decomposed into long-range Coulomb interactions ($\sum_{ij} \frac{q_i q_j}{4\pi\epsilon_0 r_{ij}}$), short-range exchange repulsion ($\sum_{ij} A_{ij} e^{-B_{ij} r_{ij}}$), and dispersion ($-\sum_{ij} S_g \frac{C_{ij}}{r_{ij}^6}$). The long-range Coulomb contribution is computed by employing the Ewald summation technique. Partial atomic charges for the framework atoms are computed using the REPEAT scheme⁴¹ with the electrostatic potentials obtained from DFT-PBE for the structure relaxation of the framework atoms. Charges for the guest molecules are taken from the guest molecule models (i.e., TIP4P-Ew, EPM2, TraPPE).^{31–34} The attraction contribution is computed using C_6 dispersion coefficients ($C_{ij} = 4\epsilon_{ij}\sigma_{ij}^6$) that are derived from UFF using Lorentz–Berthelot mixing rules for H₂O and CH₄ and from the Grimme method⁴² for CO₂. A global scaling factor, $S_g \geq 1$, is used to ensure an entirely positive-definite repulsive energy after the energy decomposition is done for each path, as the C_6 terms are assumed to give reasonable relative energies but may be off in their absolute values.

Force Field Parameterization. In decomposing the energy along each path, the point charges of all atoms in the system as well as the attractive C_{ij} terms are fixed, leaving only two parameters, A_{ij} and B_{ij} , to be fit for each pairwise interaction. Before fitting A_{ij} and B_{ij} , we create an initial guess for each pairwise interaction by mapping the UFF Lennard-Jones parameters to the Buckingham parameters. The corresponding pairwise repulsive parameters A_{ij} and B_{ij} are then optimized by a grid search method so as to minimize the difference between the DFT interaction energy and the force field energy along the approaching path for this pair. Although each path was designed to probe a specific pairwise interaction, it is impossible to eliminate interactions with the other framework atoms, and the A_{ij} and B_{ij} parameters for a given pair are thus dependent on every other pairwise interaction in the system. As a result, the fitting is done in a self-consistent manner: once the first set of two parameters is optimized for the first pairwise interaction (while holding all other pairs of parameters fixed), the second set of two parameters is optimized for the next pairwise interaction, and so on, until parameters have been fit for each pairwise interaction; we then go back and reoptimize each set of two parameters following the same order as above for *N* cycles until they reach convergence.

To determine the order in which these parameters are fit for each approaching pair, the ratio of the computed repulsive

energy between the approached pair to the total repulsive energy along a path is computed for each pairwise interaction; the A_{ij} and B_{ij} parameters are then fit sequentially for each approaching pair from the highest to lowest ratio, and repeated iteratively until all of the parameters have converged. For more details, see Lin et al.²⁹

In the case of CH_4 and CO_2 , this fitting procedure was performed for framework– $\text{C}(\text{CH}_4)$ and framework– $\text{O}(\text{CO}_2)$ interactions in M-MOF-74, with the exception of framework– $\text{C}(\text{CO}_2)$, $\text{H}(\text{framework})\text{–O}(\text{CO}_2)$, and $\text{H}(\text{framework})\text{–C}(\text{CH}_4)$ interactions. The interactions left out of the fitting procedure are instead described with a Lennard-Jones potential and the C_6 dispersion coefficients, obtained from Grimme's DFT-D2 method in the case of CO_2 .⁴² The σ parameters used in the Lennard-Jones potentials were fixed to have a value equal to the sum of the atomic van der Waal radii for each pairwise interaction. As mentioned above, except for the H-approaching path, all other paths ($\text{M, O}_a, \text{O}_b, \text{O}_c, \text{C}_a, \text{C}_b, \text{C}_c, \text{C}_d$) were included in the iterative fitting procedures for $\text{C}(\text{CH}_4)$ and $\text{O}(\text{CO}_2)$. Upon convergence of the parameters for Mg-MOF-74, the interaction parameters involving all but the metal atoms are then held fixed while reoptimizing metal– $\text{C}(\text{CH}_4)$ and metal– $\text{O}(\text{CO}_2)$ interactions for all of the other frameworks (Mn, Fe, Co, Ni, Zn).

In the case of H_2O , this procedure is repeated for fitting all framework– $\text{O}(\text{H}_2\text{O})$ interactions and some framework– $\text{H}(\text{H}_2\text{O})$ interactions. For each metal ($\text{M} = \text{Mg, Mn, Fe, Co, Ni, Zn}$), the paths included in the iterative fitting procedure were $\text{M–O}_b\text{–O}_c\text{–C}_a\text{–C}_b\text{–C}_c\text{–C}_d\text{–O}(\text{H}_2\text{O})$ and $\text{O}_b\text{–C}_b\text{–H}(\text{H}_2\text{O})$. It is worth noting that the $\text{O}_a\text{–O}(\text{H}_2\text{O})$ path was left out of the fitting procedure for all metals as including it led to no convergence in the interaction parameters. This is because the energies along the O_a path were similar in magnitude to the metal path, and it was not possible to probe the O_a interaction without having large contributions from the metal atom interactions. Because the metal and O_a parameters were highly dependent on each other, the O_a parameters were fixed so as to get a better fit for the interaction energies along metal path. $\text{H–O}(\text{H}_2\text{O})$, $\text{M–H}(\text{H}_2\text{O})$, and $\text{H–H}(\text{H}_2\text{O})$ paths were also not included in the fitting procedure. As they are very similar, interaction parameters for the same pair of atom-types in the different metal frameworks are then averaged together and fixed to the resulting values. The pairwise interaction terms involving the metal atoms are then reoptimized for each framework so as to minimize the difference between the energies computed by the force field and the energies computed from DFT along each approaching path. For the force field parameters, see Tables S4–S9.

Classical Molecular Simulations. Monte Carlo (MC) simulations are used to calculate the adsorption properties of the three gases of interest in each framework. Total interaction energies in these simulations include electrostatics, short-range repulsion, and dispersion interactions, computed using the force field parameters obtained as described above. The nonelectrostatic potentials are truncated and shifted to zero at a cutoff radius of 12.8 Å. Ewald summations are used to compute long-range Coulomb contributions. The simulation box is composed of multiple unit cells such that the distances between two successive planes of (1,0,0), (0,1,0), and (0,0,1) are at least twice the cutoff radius. For any interactions not parametrized by our force fields, Lennard-Jones + Coulomb potentials were used with Lorentz–Berthelot mixing rules. These parameters were from the UFF force field, the respective

guest models for CH_4 and H_2O , and from Grimme's method⁴² for CO_2 . Details regarding the force field parameters used herein are given in Tables S4–S9.

Metal–Organic Framework Synthesis. All reagents were obtained from commercial vendors and used without further purification. $\text{Mn}_2(\text{dobdc})$, $\text{Cu}_2(\text{dobdc})$, $\text{Fe}_2(\text{dobdc})$, and $\text{Zn}_2(\text{dobdc})$ were synthesized according to literature procedures.^{10,12,43,44} $\text{Mg}_2(\text{dobpdc})$ was also synthesized and activated according to the literature procedure.⁴⁵ The successful synthesis and activation of the compounds was confirmed by comparing the X-ray powder diffraction patterns and Langmuir surface areas to those previously reported.

Low-Pressure CO_2 Adsorption Measurements. Low-pressure (0–1.2 bar) isotherm measurements were completed; approximately 100 mg of activated sample in an ASAP tube equipped with a Transeal was placed on the analysis port of a Micromeritics ASAP 2020 equipped with an HD transducer. The surface area was measured on the sample in the ASAP tube with an isothermal jacket in liquid N_2 (77 K) and calculated with the Micromeritics software. CO_2 and CH_4 isotherms were measured on the ASAP 2020 HD instrument as well, with temperature control via a Julabo circulating water bath.

High-Pressure CH_4 and CO_2 Adsorption Measurements. High-pressure CH_4 and CO_2 adsorption isotherms in the range of 0–90 and 0–50 bar, respectively, were measured on an HPVA II 100 from Particulate Systems, a Micromeritics company. In a typical measurement, 0.5–1.0 g of activated sample was loaded into a tared stainless steel sample holder inside a glovebox under a N_2 atmosphere. Prior to connecting the sample holder to the VCR fittings of the complete high-pressure assembly inside the glovebox, the sample holder was weighed to determine the sample mass. The sample holder was then transferred to the HPVA-II-100, connected to the instrument's analysis port via an OCR fitting, and evacuated at room temperature for at least 2 h. The sample holder was placed inside an aluminum recirculating dewar connected to a Julabo FP89-HL isothermal bath filled with either Julabo Thermal C2 fluid or Syltherm from Dow Chemical. The temperature stability of the isothermal bath is ± 0.02 °C. Methods for accurately measuring the relevant sample freespace, which involve the expansion of He from a calibrated volume at 0.7 bar and 25 °C to the evacuated sample holder, were described in detail previously.⁴⁶ Nonideality corrections were performed using the CH_4 and CO_2 compressibility factors tabulated in the NIST REFPROP database at each measured temperature and pressure.⁴⁷

■ RESULTS AND DISCUSSION

I. Fitting the Guest–Framework Interactions. We first derived a force field for CO_2 adsorption in M-MOF-74 ($\text{M} = \text{Mg, Fe, Co, Ni, and Zn}$). We use the EPM2³¹ model for CO_2 molecules and UFF force field parameters for the framework atoms as a starting point. The derived force field for CO_2 in M-MOF-74 nicely reproduces our DFT energies. As an example, the resulting force field nicely reproduces DFT energies along all of the paths for Co-MOF-74 as shown in Figure 1. Single point energies along the various approaching paths for Fe- and Ni-MOF-74 are available in Figures S2 and S3, and illustrate the agreement between the DFT-derived force field and the DFT energies along all of the paths for these frameworks as well. For a comparison of single point energies in Mg- and Zn-MOF-74, see Lin et al.²⁹ Although UFF was intended to be a very generalizable force field, it was not parametrized with

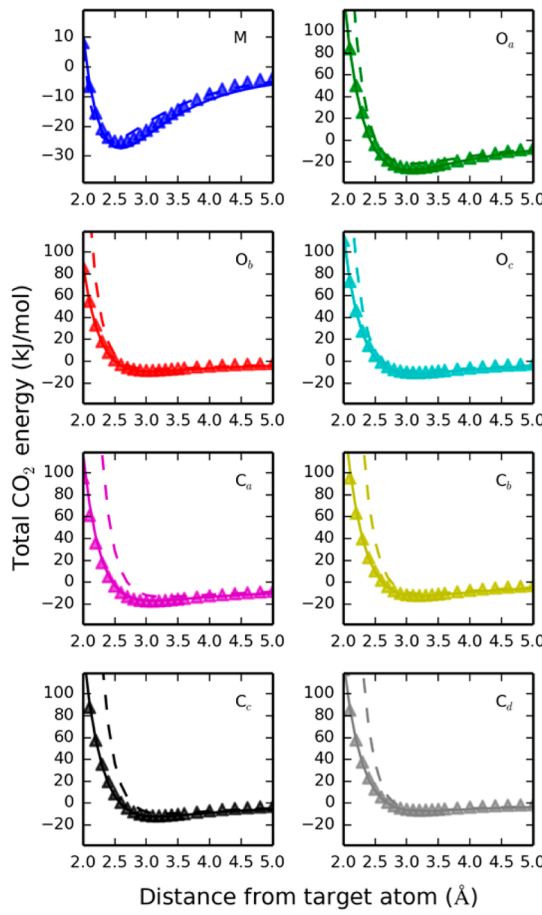


Figure 1. Comparison of CO₂–framework interaction energies in Co-MOF-74 obtained from the DFT calculations (triangular markers), the DFT-derived force field (solid line), and the UFF force field (dashed line) along the various approaching paths.

metal sites in the training set that were similar enough to the metal sites present in MOF-74, and as a result the model does not necessarily predict the energetics of these systems accurately. The way this inaccuracy is manifested in MOF-74 is that UFF tends to overestimate the repulsion from guests at short distances in the entire series of frameworks. Indeed, this is one of the reasons why UFF fails to accurately model the gas adsorption properties of MOF-74, as it leads to an under-prediction of the various gases' binding energies in the frameworks such that the adsorption capacities of MOF-74 for various flue gas components are considerably underestimated. Parameters for Mn were also fit originally, but the fitted potential led to unrealistic uptake at low pressures (<10 Pa). The force field energies for CO₂ in Mn-MOF-74 did indeed match the DFT energies after fitting, and as such we believe that it is not a poor fit that led to a prediction of unrealistic CO₂ uptakes. The reasons behind this phenomenon could actually be quite complicated, perhaps due to the use of the Buckingham potential or Grimme's C₆ correction. Therefore, we chose to leave Mn-MOF-74 out of the CO₂ reparameterization such that a working Mn potential for CO₂ obtained using the method outlined in this Article is not available at this moment.

We then derived a force field for H₂O adsorption in M-MOF-74 (M = Mg, Mn, Fe, Co, Ni, Zn). We use the TIP4P-Ew^{33,34} model for H₂O molecules and UFF force field parameters for the framework atoms to start off.³³ The

resulting force field nicely reproduces DFT energies along all of the O(H₂O) and H(H₂O) approaching paths considered for Co-MOF-74 (shown as an example in Figure 2). Additionally, a

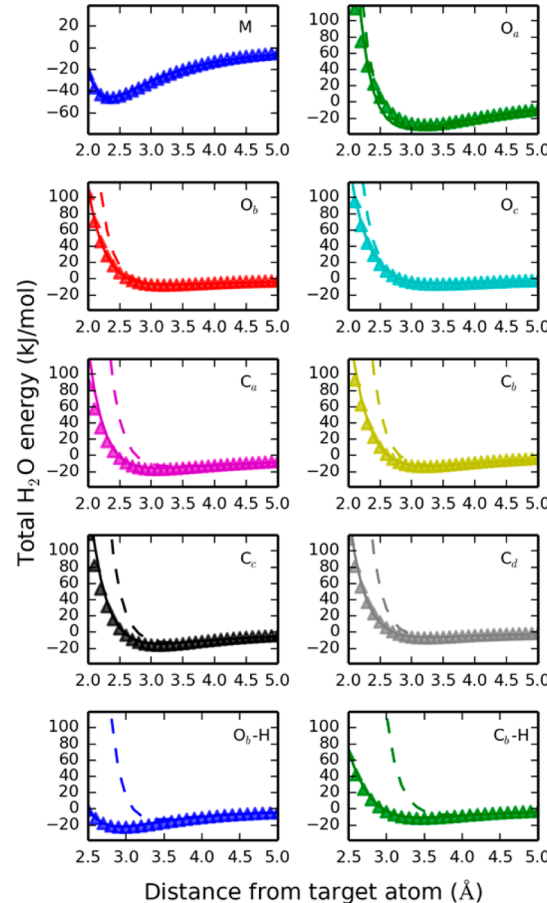


Figure 2. Comparison of H₂O–framework interaction energies in Co-MOF-74 obtained from the DFT calculations (triangular markers), the DFT-derived force field (solid line), and the UFF force field (dashed line) along the O(H₂O) approaching paths (top eight) and H(H₂O) approaching paths (bottom two).

comparison of single point energies for Mn-, Fe-, and Ni-MOF-74 along the various approaching paths for H₂O is available in Figures S12–S14. For a comparison of single point energies in Mg- and Zn-MOF-74, see Lin et al.²⁹

We then derived a force field for CH₄ adsorbed in M-MOF-74 (M = Mg, Mn, Fe, Co, Ni, Zn). We use the TraPPE³² model for CH₄ molecules and UFF force field parameters for the framework atoms to begin.⁴⁸ The resulting force field nicely reproduces DFT energies along all of the paths for Co-MOF-74, shown as an example in Figure 3. Moreover, a comparison of single point energies along all approaching paths for Mg-, Mn-, Fe-, Ni-, and Zn-MOF-74 is available in Figures S21–S25. Comparison with the energies computed using the UFF force field once again shows using the UFF force field leads to an overprediction of the short-range repulsion and, as a result, noticeably smaller values for the interaction energies along each path.

We obtained very reasonable agreement for the guest–framework interaction energies for all gases and MOFs. Most notably, we obtain a poorer overall fit for the CH₄ DFT energies than for the other two guests. We see that for CH₄, the energies computed using the derived force field do not

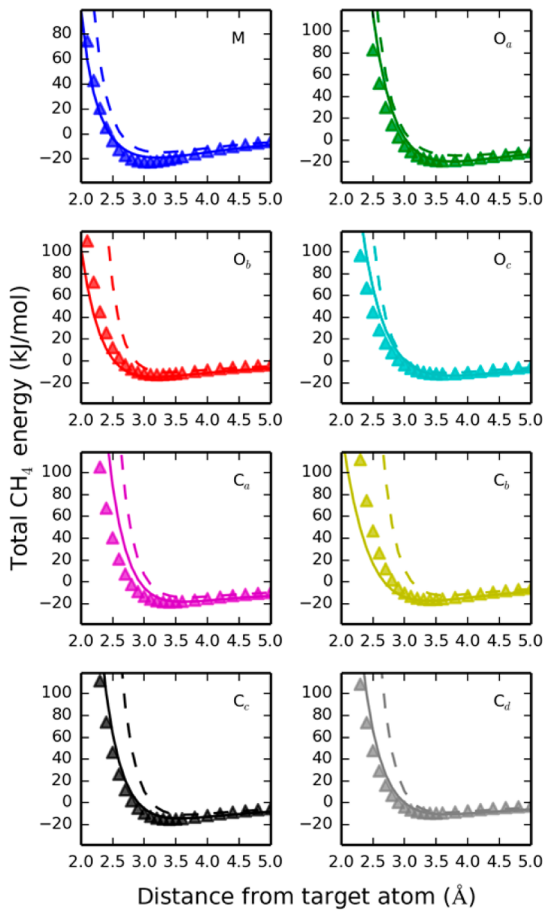


Figure 3. Comparison of CH_4 -framework interaction energies in Co-MOF-74 obtained from the DFT calculations (triangular markers), the DFT-derived force field (solid line), and the UFF force field (dashed line) along the various approaching paths.

reproduce the very minimum DFT energy along the metal paths, although away from this minimum the energies are reproduced quite well. In the worst cases, the minima along a given metal path deviate from the DFT minima by roughly 6 kJ/mol, or about 25% of the total binding energy. The energies along the other (non-metal) CH_4 paths, however, are well reproduced using the DFT force field in all frameworks, with

the exception of Co-MOF-74 path energies, which exhibit relatively poor agreement below 3.0 Å. Moreover, the fits for CO_2 are generally better than for H_2O , as the derived force field does not always reproduce the minimum DFT energy along each of the H_2O paths. Nonetheless, the DFT-derived force field energies are generally in good agreement with the calculated DFT energies, and in all cases a significant improvement from energies computed using UFF.

II. Gas Adsorption in M-MOF-74. II.a. CO_2 . The total adsorption isotherms are computed using the DFT-derived force field and compared to the experimental isotherms for CO_2 in M-MOF-74 (Figure 4).¹² For this family of MOFs, it has been established via the isosteric heats of adsorption and X-ray diffraction data that 20–30% of the metal sites are inaccessible in some MOF-74 structures.¹² There are many methods by which isotherms are commonly scaled as a way to account for structural defects in synthesized materials and thus allow for a clearer comparison between the computed and measured isotherms.^{28,29,49–51} For simplicity, we scaled all of the computed isotherms by 85% regardless of the framework as approximately this percentage of metal sites is accessible in each synthesized framework. A comparison between isotherms computed using the UFF force field and the experimental isotherms for CO_2 in these same frameworks can also be found in Figure 4. The unmodified computed isotherm data at 287, 298, and 313 K are available in Figures S4–S6. As expected, lowering the temperature leads to a higher loading over the entire pressure range considered.

With our new DFT-derived force field, the predicted CO_2 isotherms are in good agreement with the experimental isotherms, especially at lower pressures. Below 0.6 bar, the trend in the isotherms (ordered by decreasing CO_2 uptake: Mg, Ni, Co, Fe, Zn) is accurately reproduced with the DFT-derived force field but not with the UFF force field. Of the computed isotherms, predictions for CO_2 in Ni-MOF-74 deviate the most from the experimental measurements, but it should be noted that the isotherm computed using the DFT-derived force field is in significantly better agreement with the experimental results than the isotherm computed using the UFF force field. While this difference could arise from a number of factors (including unavoidable defects in the crystalline structure), it is certainly possible that the electronic structure at the Ni center is described less accurately than the other metals simply due to

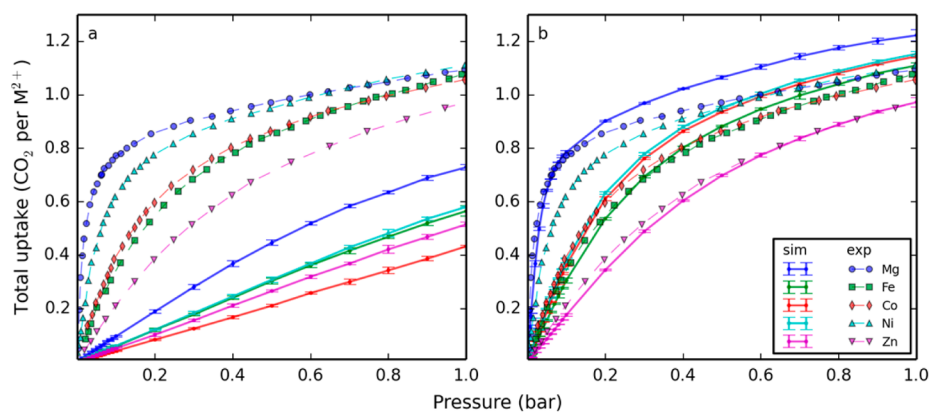


Figure 4. Comparison between the experimental and simulated isotherms using the UFF and EPM2 force fields (a) and the DFT-derived force field (b) for CO_2 inside M-MOF-74 at 298 K. The experimental data of Queen et al.¹² are shown by the large geometric markers and dashed lines, whereas the corresponding scaled isotherms from simulation are shown by solid lines. Error bars are plotted for simulation data but smaller than the markers in most cases.

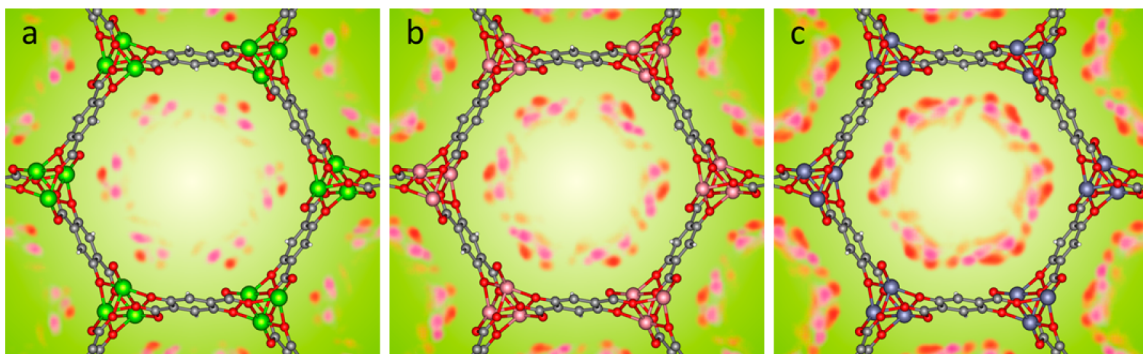


Figure 5. Probability density plots computed using the DFT-derived force field for CO_2 in (a) Mg-, (b) Co-, and (c) Zn-MOF-74, respectively, at 100 K. Orange clouds represent the density corresponding to the oxygen atoms in CO_2 , whereas magenta clouds correspond to the density from the carbon atoms. Darker colors correspond to a higher probability of finding a guest at those positions. Each colored sphere corresponds to the following atoms: C, gray; O, red; H, white; Mg, lime green; Co, pink; Zn, slate.

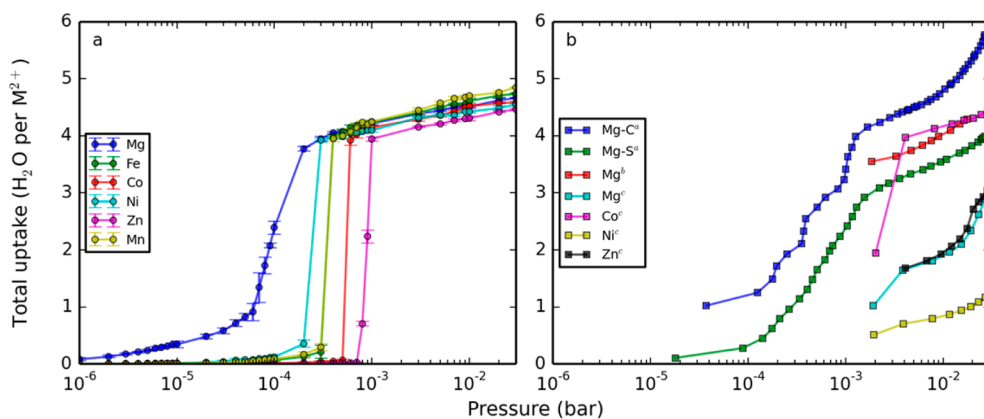


Figure 6. Comparison between adsorption isotherms computed using the DFT-derived force field (a) and experimentally measured (b) for H_2O inside M-MOF-74 at 298 K. The experimental data of Yang et al.,^{a,5} Schoenecker et al.,^{b,53} and Glover et al.^{c,54} are shown for the various metal frameworks studied. Error bars are plotted for simulation data but smaller than the markers in most cases.

the level of theory employed. For example, recall that the Hubbard- U correction is used for these systems and the U value for Ni is quite high (6.4). In view of that, we wish to stress that the performance of any ab initio force field is dependent on the level of theory used.

A comparison of probability densities computed for 216 CO_2 molecules inside each M-MOF-74 framework (corresponding to 1.5 guest molecules per metal site) using the DFT-derived force field (Figure 5) and neutron powder diffraction (NPD) experiments¹² shows that our force field can reproduce experimental observations. All probability density plots were created using PEGrid and VisIt⁵⁵ by binning positions of guest molecules from three (for CO_2 and CH_4) and ten (for H_2O) 100 000 cycle $N-V-T$ simulations into $0.2 \times 0.2 \times 0.2 \text{ \AA}^3$ voxels. The appearance of two major CO_2 binding sites under these conditions, with the first being the stronger and more occupied binding site at the metal and the second weaker site lying nearly parallel to the channel walls between two of the primary sites, is clearly captured by our simulations.

Some of the key differences between CO_2 adsorption in the different metal frameworks are highlighted in Figure 5. In Mg-MOF-74, the framework with the largest affinity for CO_2 , the probability density illustrates how any adsorbed CO_2 is significantly less mobile than in both Co- and Zn-MOF-74. Similarly, the secondary binding sites are less apparent in Mg-MOF-74 than in the other frameworks. This suggests that due to the larger difference in energy between the primary and

secondary sites, all of the primary binding sites must be occupied, while only one-half of the secondary ones are filled in Mg-MOF-74; on the other hand, in Co- and Zn-MOF-74 the secondary binding sites are significantly more occupied due to the secondary and primary binding sites being closer in energy. In Zn-MOF-74, the framework with the lowest binding energy for CO_2 of all of the frameworks studied, a more extensive distribution in the binding site occupancy is apparent along the surface of the framework in addition to a higher mobility indicated by the broadness of the observed density clouds. Additional probability density maps for all of the metal frameworks studied can be found in Figures S7–S11.

II.b. H_2O . The total adsorption isotherms computed using the DFT-derived force field for H_2O in M-MOF-74 are shown in Figure 6 along with experimentally measured isotherms from the literature. Using our model, we observe a trend in step of the computed isotherms related to heat of adsorption, which is not observed experimentally. The greater is the binding energy for H_2O at the metal site, the sooner the step in the isotherm occurs. We also observe a slightly different mechanism for H_2O adsorption in Mg-MOF-74, in which H_2O has the largest binding energy, than in the other five frameworks. The gradual increase in uptake at low pressures followed by the sharp increase in uptake after the uptake reaches $\sim 1 \text{ H}_2\text{O}$ per M^{2+} suggests that due to the large binding energy, all of the metal sites become occupied first such that the metal– H_2O interaction is stronger than H_2O – H_2O interactions, but that

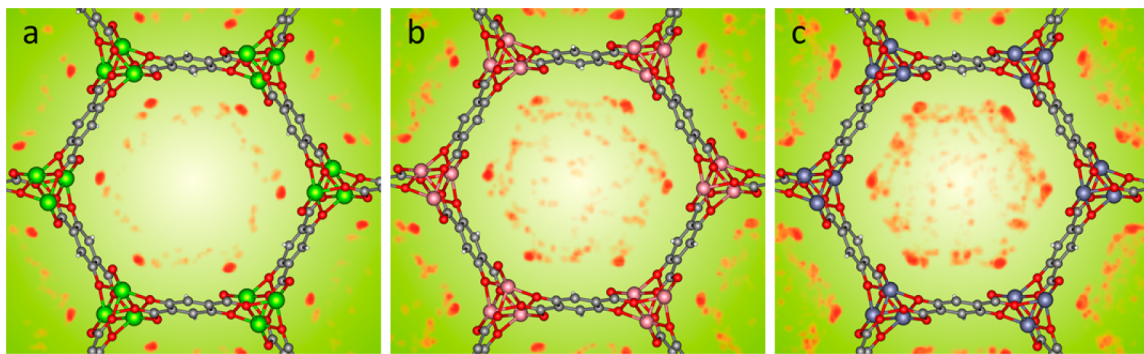


Figure 7. Probability density plots computed using the DFT-derived force field for H_2O in (a) Mg-, (b) Co-, and (c) Zn-MOF-74, respectively, at 100 K. Orange clouds represent the density corresponding to the oxygen atoms in H_2O . Darker colors correspond to a higher probability of finding a guest at those positions. Each colored sphere corresponds to the following atoms: C, gray; O, red; H, white; Mg, lime green; Co, pink; Zn, slate.

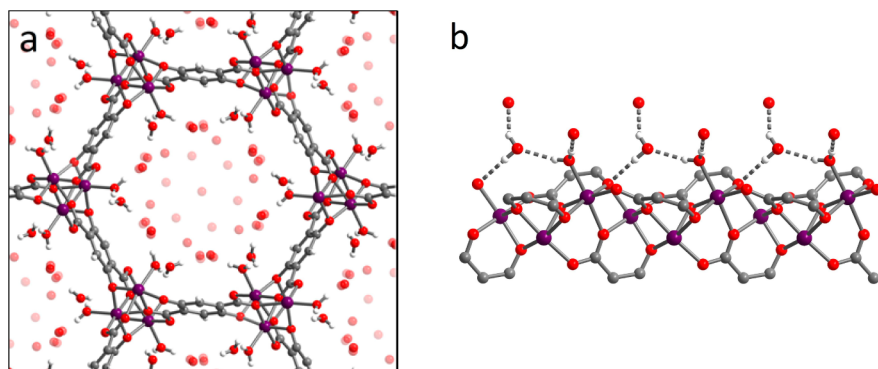


Figure 8. XRD crystal structure with disorder for Co-MOF-74 framework saturated with H_2O at 100 K. (a) View down the pores of the channel. (b) View along the c -axis of one metal chain. Each colored sphere corresponds to the following atoms: C, gray; O, red; H, white; Co, purple.

once all of the metal sites are occupied $\text{H}_2\text{O}-\text{H}_2\text{O}$ interactions take over and H_2O condenses into the pores giving rise to the inflection. On the other hand, for the five other frameworks, H_2O adsorption is much less than 1 H_2O per M^{2+} right before the inflections in the isotherms occur, suggesting that once a single H_2O molecule binds in each framework it becomes more favorable to add another H_2O molecule right next to it, thus leading to H_2O condensation in the pores.

One of the challenges with studying H_2O adsorption in these frameworks, perhaps due to the large H_2O binding energies and/or H_2O behavior in a confined environment, is that experimentally it is difficult to accurately and reliably measure adsorption isotherms, and isotherms collected for the same metal framework are often in stark disagreement between different groups or even different samples. Although the lack of conclusive adsorption isotherms for H_2O in the various MOF-74 frameworks studied here prevents us from evaluating the predictive power of our obtained H_2O force field, it is worth noting the differences between the multistep character observed in the measured isotherms and the single-step character predicted by our model. Nonetheless, the purpose of deriving this force field for H_2O was not to study single-component H_2O adsorption in MOFs, but to be better equipped to study the separations of other gases from wet mixtures where H_2O is present in negligible amounts. As such, we expect our force field to be suitable for this type of analysis, as our force field was parametrized to DFT binding energies for one H_2O molecule in the framework at a time and thus should be more accurate at lower concentrations of H_2O where $\text{H}_2\text{O}-\text{H}_2\text{O}$ interactions do not play a dominant role. With regards to the choice of the

initial H_2O model (TIP4P-Ew³³), we initially considered other nonpolarizable H_2O models (i.e., SPC, SPC/E, TIPnP, TIPnP-Ew) due to their simple potential forms.^{33,34,55–62} Many groups have analyzed the performance of different H_2O models in Mg-MOF-74,⁶³ and it has been shown that models with more than three sites provide better quantitative agreement with predicted binding geometries from DFT calculations, and that five-site models give the best agreement.⁶⁴ However, in grand canonical Monte Carlo simulations, the TIPSP-Ew model shows a very different adsorption mechanism as compared to TIP4P-Ew, which is not observed in experimental data. For these reasons, the TIP4P-Ew model was chosen over the other models considered. In addition, adsorption isotherms computed using the TIP4P-Ew model and UFF to study H_2O adsorption in Mg-MOF-74 show a saturation of the framework at lower pressures than TIP3P and TIPSP-Ew, as well as the higher uptake after the step in the isotherm occurs.^{63,64} This last observation makes it attractive to use for the purposes of studying separations of wet gas mixtures in M-MOF-74 as using this water model would provide a loose upper-bound from simulation for each framework's sensitivity to H_2O .

Another challenge when modeling H_2O adsorption in these frameworks stems from any substantial rearrangements in the framework structure, which come about as a result of H_2O adsorption. Our force field will be more accurate in the limit that the framework does not distort much upon H_2O binding, and in the limit that the chosen H_2O model is adequate at describing the H_2O in the pores at higher pressures.

A comparison of probability densities computed for 216 H_2O molecules inside the M-MOF-74 frameworks using the DFT-

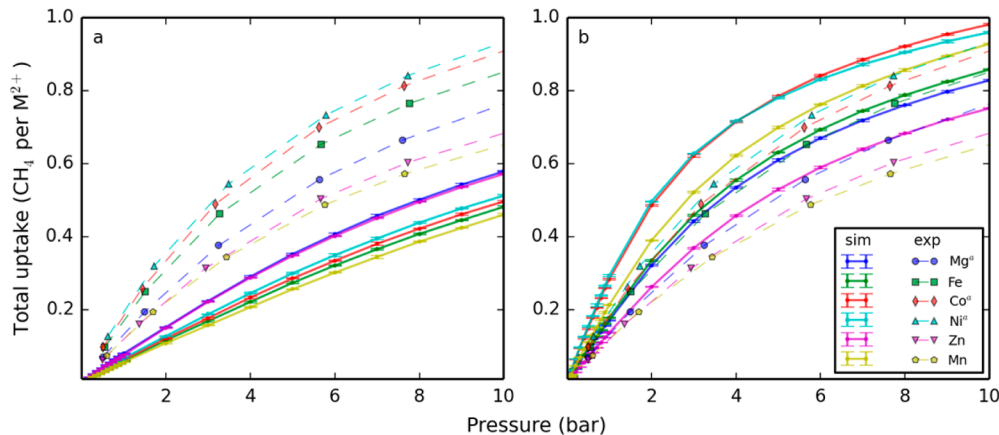


Figure 9. Comparison between the experimental and simulated isotherms computed using the UFF and TraPPE force fields (a) and the DFT-derived force field (b) for CH_4 in M-MOF-74 at 298 K. The experimental data of Mason et al.⁴⁶ are shown by the geometric markers and dashed lines for the Mg, Co, and Ni frameworks. Isotherms were measured in this work for the Fe, Zn, and Mn frameworks for comparison with simulation. The corresponding scaled isotherms from simulation are shown by the solid lines. Error bars are plotted for simulation data but in most cases smaller than the markers.

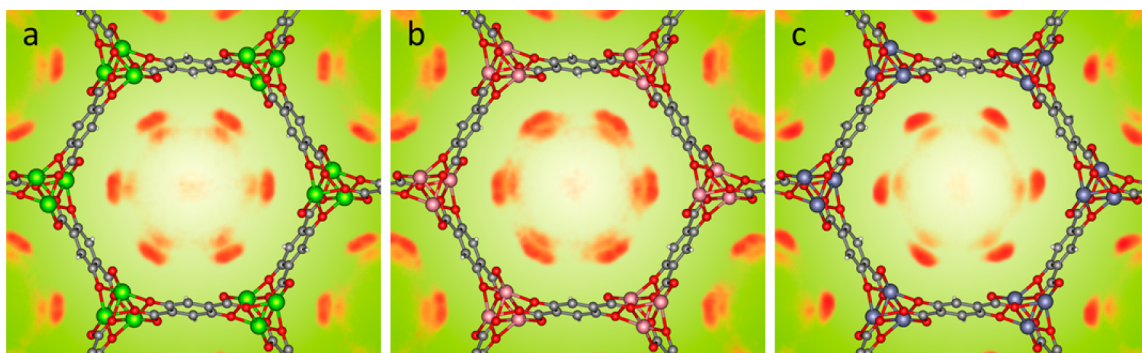


Figure 10. Probability density plots computed using the DFT-derived force field for CH_4 in (a) Mg-, (b) Co-, and (c) Zn-MOF-74, respectively, at 100 K. Orange clouds represent the density corresponding to the carbon atoms in CH_4 . Darker colors correspond to a higher probability of finding a guest at those positions. Each colored sphere corresponds to the following atoms: C, gray; O, red; H, white; Mg, lime green; Co, pink; Zn, slate.

derived force field (Figure 7) and binding geometries obtained from single-crystal X-ray diffraction (XRD) experiments (Figure 8) shows that with our DFT-derived H_2O force field, we are able to reproduce the experimentally observed oxygen positions for guest H_2O molecules in Co-MOF-74. We observe the appearance of the multiple binding sites seen experimentally, the most occupied being that over the metal center, followed by many others both along the walls of the channels and near the centers of the pores. From the computed probability densities, it is evident that there is significant disorder in the secondary binding sites. This disorder in the secondary binding sites manifests itself as many little clouds of high density as opposed to the broad clouds observed for CO_2 , indicating that there are many local minimums in the way water can arrange itself in the pores at these conditions, and once a configuration finds such a minimum the water molecules rarely move. Configurations would have to be sampled for significantly longer at 100 K to see an adequate distribution of the secondary binding sites. Nonetheless, disorder in the secondary sites is also observed experimentally, where in the solved structure certain water molecules are disordered over multiple positions as shown in Figure 8a. The appearance of these secondary binding sites is not observed when using the UFF force field.

Some of the differences between H_2O adsorption in the different metal frameworks, with similar trends to those observed in CO_2 adsorption, are also highlighted in Figure 7. In Mg-MOF-74, which has the largest affinity for H_2O of all six frameworks studied, the secondary, tertiary, and weaker binding sites are significantly less apparent than in the other frameworks, suggesting once again that all of the primary binding sites are fully occupied while the other sites are only partially occupied at these conditions. However, in Co-MOF-74, the weaker binding sites are significantly more occupied. In Zn-MOF-74, the framework with the weakest binding affinity for H_2O at the metal site of the three frameworks shown in Figure 7, the weaker binding sites have a higher occupancy still. This is in sharp contrast to what is observed when using the UFF force field, where the water spends the majority of its time at or near the metal site for all frameworks studied in this work. Additional probability density maps for all of the metal frameworks studied can be found in Figures S15–S20.

II.c. CH_4 . We now compare the total adsorption isotherms computed using the DFT-derived force field with the experimental isotherms for CH_4 in M-MOF-74 (Figure 9). Because not all of the metal sites are accessible, the computed isotherms were again scaled down to 85%. A comparison between the isotherms computed using the UFF force field and the experimental isotherms for CH_4 in these same frameworks

can also be found in Figure 9. Unscaled CH₄ isotherms computed at 287, 298, and 313 K are available in Figures S26–S28.

With our new DFT-derived force field, the calculated isotherms are in good agreement with the experimental isotherms, especially at lower pressures. The experimentally observed trends are also reproduced using our simulations at lower pressures (ordered by decreasing CH₄ uptake at 1 bar: Ni > Co > Fe > Mg > Zn), except in the case of Mn-MOF-74, which we predict to have a CH₄ uptake between Fe and Co at 1 bar but is experimentally observed to have one of the lowest uptakes. At this level of theory, this suggests an incomplete activation and higher fraction of inaccessible metal sites in the as-synthesized Mn-MOF-74 crystals.

A comparison of probability densities computed for 216 CH₄ molecules inside three different M-MOF-74 frameworks using the DFT-derived force field is shown in Figure 10. In the case of CH₄, we see exactly three binding sites in all six frameworks at 100 K. Furthermore, the CH₄ molecule appears less localized than both CO₂ and H₂O at this primary binding site, an observation that is supported by the significantly weaker binding energy of CH₄ in all MOF-74 frameworks as compared to the two other guests.

Differences in CH₄ adsorption in the six different metal-organic frameworks studied are also more subtle when compared to the adsorption behavior of the other guests; this is not surprising because the differences in the binding energies and in the adsorption isotherms are also smaller. As mentioned above, three distinct binding sites are apparent in each framework, with the primary binding site centered around the metal, a secondary binding site adjacent to the primary site (further inside the pore and slightly offset in the z-direction), and a tertiary site right in the center of the pore. In frameworks where there is a stronger interaction between the methane and the ligand atom-types, the densities of the primary and secondary binding sites are wider and more spread out along the channel walls, as expected. Additional probability density maps for all of the metal frameworks studied can be found in Figures S33–S38.

III.d. N₂, N₂ isotherms computed at 287, 298, and 313 K using the UFF force field for the framework and the TraPPE³² force field for the guest atoms are given in Figures S39–S41. While this gas is of interest for studying gas separations in certain gas compositions, the UFF and TraPPE force fields are adequate for modeling adsorption in these frameworks. Because the binding energy is not underestimated to as great of an extent when using the UFF force field to study N₂ adsorption in simulations as it is for CO₂ and H₂O, we did not reparameterize N₂.

III. Mixture Adsorption in M-MOF-74. Below we show two different examples of gas mixtures, which we can study using our force fields. In theory there exists a large number of combinations of gases and conditions, which could be relevant for a specific application, especially considering that different power plants would operate under a range of optimal conditions. To be the most relevant and minimize the number of calculations, we have carefully chosen to study the separations below. We have studied CO₂/H₂O adsorption at a fixed temperature and pressure with varying compositions of CO₂ and H₂O so as to consider the H₂O sensitivity of these frameworks, something that would be relevant for carbon capture from wet flues. We also studied the adsorption of dry N₂/CO₂/CH₄ gas mixtures at a composition of 5% N₂, 10%

CO₂, and 85% CH₄ at two temperatures and a range of pressures as these would be relevant to carbon capture applications from both natural gas and coal-fired power plant flue gases.

III.a. CO₂/H₂O. By computing binary mixture isotherms of CO₂ and H₂O in the various frameworks, we can study the frameworks' sensitivity to H₂O under conditions relevant for CO₂ capture from postcombustion flue gas. For all five frameworks, we looked at CO₂ uptake versus an increasing H₂O mole fraction in a binary mixture of CO₂ and H₂O (Figure 11). We observed that the positions of the inflection points in

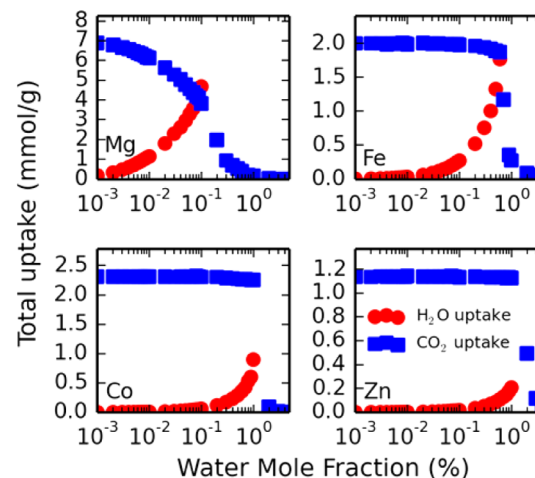


Figure 11. Computed CO₂/H₂O mixture isotherms in Mg-MOF-74 (top left), Fe-MOF-74 (top right), Co-MOF-74 (bottom left), and Zn-MOF-74 (bottom right) at 313 K and 0.15 bar, illustrating the drop in CO₂ uptake with increasing H₂O mole fraction in the reservoir. The red circular markers symbolize H₂O adsorption, whereas the blue square markers symbolize CO₂ adsorption.

these mixture isotherms are correlated to the binding energy for H₂O in the framework. In other words, the larger is the binding energy for H₂O, the lower is the H₂O mole fraction at which CO₂ uptake decreases. For example, in Mg-MOF-74, the framework with the largest DFT binding energy (-66.9 kJ/mol), H₂O uptake is greater than CO₂ uptake in the framework at a mere 0.1% mole fraction of H₂O in the gas reservoir under conditions of 313 K and 0.15 bar. Conversely, in Zn-MOF-74, the framework with the weakest H₂O binding energy from DFT (-46.3 kJ/mol), H₂O uptake becomes greater than CO₂ uptake in the framework when the mole fraction of H₂O increases to 2% under the same conditions. All of the other frameworks (M = Fe, Co, and Ni) perform somewhere in between. While Zn-MOF-74 can tolerate an order of magnitude more of H₂O than Mg-MOF-74 before becoming completely useless for carbon capture purposes, most flue gases are composed of significantly more than 2% H₂O (at 40 °C, assuming nearly complete H₂O saturation, the partial pressure of H₂O would be approximately 74 mbar, meaning most flue gases would have an H₂O mole fraction of about 7%). Thus, none of the MOF-74 frameworks mentioned above are likely suitable for carbon capture applications from any wet sources. This is in agreement with recently reported CO₂/N₂/H₂O equilibrium adsorption isotherms.³⁰ However, our simulations are able to show exactly how quickly CO₂ uptake is expected to decrease in the presence of H₂O, which is something that cannot be explicitly determined from the multicomponent

isotherm measurements without difficulty. For $\text{CO}_2/\text{H}_2\text{O}$ mixture isotherms in Ni-MOF-74, see Figure S45.

We did not analyze the separation performance of MOF-74 for wet binary mixtures containing N_2 nor CH_4 , as they are weaker binding gases than CO_2 and we expect H_2O to saturate the framework at even lower mole fractions than in the case of the $\text{CO}_2/\text{H}_2\text{O}$ binary mixtures.

III.b. $\text{N}_2/\text{CO}_2/\text{CH}_4$. Three-component mixture isotherms were also computed at 313 K and with a typical natural gas reservoir composition of 5% N_2 , 10% CO_2 , and 85% CH_4 , conditions that would be relevant for the purification of natural gas streams using pressure-swing adsorption technology.⁶⁵ We find that all of the metal frameworks adsorb significantly more CO_2 than the two other gases, with Mg-MOF-74 unsurprisingly being the most selective for CO_2 (Figure 12). We also find that lowering

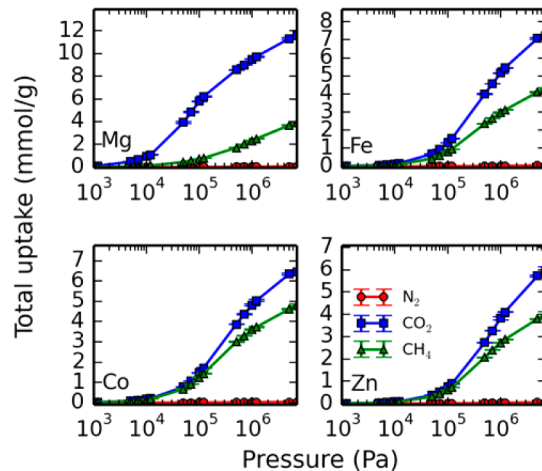


Figure 12. Computed $\text{N}_2/\text{CO}_2/\text{CH}_4$ mixture isotherms in Mg-MOF-74 (top left), Fe-MOF-74 (top right), Co-MOF-74 (bottom left), and Zn-MOF-74 (bottom right) at 313 K. The red circular markers symbolize N_2 adsorption, the green triangular markers symbolize CH_4 adsorption, and the blue square markers symbolize CO_2 adsorption. The mole fraction of gases in the reservoir is fixed at all pressures to 0.05 N_2 , 0.1 CO_2 , and 0.85 CH_4 .

the temperature dramatically improves the ratio of CO_2 adsorbed (see Figure S46). These materials are promising for natural gas purification as they adsorb significantly more CO_2 than CH_4 despite the CO_2 being present at a much lower concentration in the gas mixture. Notably, Mg-MOF-74 has a higher ratio of CO_2 to CH_4 adsorbed at all pressures than all of the other frameworks studied. Using our force field, mixtures of even greater complexity could be analyzed in these and similar frameworks.

IV. Transferability: Gas Adsorption in $\text{M}_2(\text{dobpdc})$. While these parameters are fit specifically for MOF-74 structures, we expect that they should remain valid for MOF-74 analogues. Therefore, we compute the adsorption of the different guests in the family of extended MOF-74 structures, $\text{M}_2(\text{dobpdc})$ ($\text{M} = \text{Mg}, \text{Mn}, \text{Fe}, \text{Co}, \text{Ni}, \text{Zn}$; $\text{dobpdc}^{4-} = 4,4'$ -dioxido-3,3'-biphenyldicarboxylate). This family of framework is very similar to MOF-74, the main difference being the larger pores due to the slightly longer linker, which possesses two phenyl rings instead of one. We show here the results of gas adsorption in these frameworks from simulations using our force fields.

It should be noted that while we expect our force fields to remain accurate for frameworks possessing similar character-

istics to MOF-74 (i.e., open-metal sites, 1D hexagonal channels), we do not expect them to be valid models for frameworks, which do not possess these characteristics and which differ significantly in their chemical environments. That is, the more different a structure is from MOF-74, the less accurate our force field will be at capturing the appropriate energies of the system. Furthermore, if the structure of the framework varies significantly during adsorption, or if it is known to be considerably flexible, then our rigid model will also not be suitable for modeling such a system. These aspects should be considered before deciding whether or not our models are appropriate for use in simulations of gas adsorption in a given framework, but deciding when a system is “different enough” will be left to the discretion of the user.

At the moment it is not known whether the framework distorts upon the adsorption of gases, something that could have a significant impact on the adsorption behavior of $\text{M}_2(\text{dobpdc})$, especially at higher pressures. We believe our predictions to be correct in the limit that the $\text{M}_2(\text{dobpdc})$ frameworks do not distort significantly during gas adsorption as we are using a rigid approximation. In addition, as in the case of the MOF-74 frameworks, we expect our predictions to be most accurate below loadings of one molecule per metal site.

To maintain neutral frameworks, atomic charges in the various $\text{M}_2(\text{dobpdc})$ structures are obtained using the Rappe–Goddard charge equilibration method (QEeq⁶⁶) with reoptimized parameters. Among parameters for QEeq method, the atomic electronegativity (χ) and hardness (J) for each atom-type are reoptimized by minimizing the error between QEeq- and REPEAT-derived charges, while employing the decay parameters for a single normalized s-type Slater orbital from the OpenBabel software.⁶⁷ The QEeq parameters for all elements were optimized with the exception of hydrogen parameters, which were fixed to the original values.⁶⁶ Our QEeq parametrization was trained to reproduce REPEAT charges in six different M-MOF-74 ($\text{M} = \text{Mg}, \text{Mn}, \text{Fe}, \text{Co}, \text{Ni}, \text{Zn}$) frameworks. The QEeq parametrization was performed with our in-house optimization code by minimizing the summation of the differences between the REPEAT charges and the new charges from the QEeq formalism for the whole training set. Reoptimized parameters are summarized in Table S10.

IV.a. CO_2 . Computed total CO_2 adsorption isotherms in $\text{M}_2(\text{dobpdc})$ frameworks using the DFT-derived force field are available in Figure S47. When comparing with M-MOF-74 results (Figure 13), we observe very similar uptakes in $\text{M}_2(\text{dobpdc})$ at very low pressures. That is, below 0.1 bar, the isotherms for the same metal in the regular and extended frameworks are almost overlapping, with only a slightly higher uptake observed in each respective MOF-74 framework. However, above 1 bar, the isotherms for the two sets of frameworks diverge significantly, with $\text{M}_2(\text{dobpdc})$ frameworks exhibiting a much larger uptake than the MOF-74 frameworks. Furthermore, CO_2 isotherms in all $\text{M}_2(\text{dobpdc})$ frameworks exhibit triple-site Langmuir behavior, as opposed to the dual-site Langmuir behavior observed in MOF-74 frameworks.

Simulation results for CO_2 adsorption in $\text{Mg}_2(\text{dobpdc})$ using the DFT-derived force field are compared to experimental measurements in Figure 14. Furthermore, the heats of adsorption for CO_2 in $\text{Mg}_2(\text{dobpdc})$ computed using the DFT-derived FF and the UFF force field are compared to experimental measurements in Figure 15. We find that while the computed and measured isotherms are in good agreement at low pressures, the experimentally obtained heats of

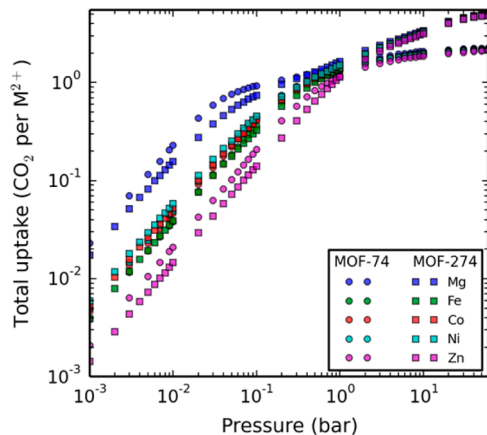


Figure 13. Comparison of CO₂ adsorption isotherms computed at 298 K using the DFT-derived force field in MOF-74 (circular markers) and M₂(dobpdc) (square markers) frameworks on a logarithmic plot.

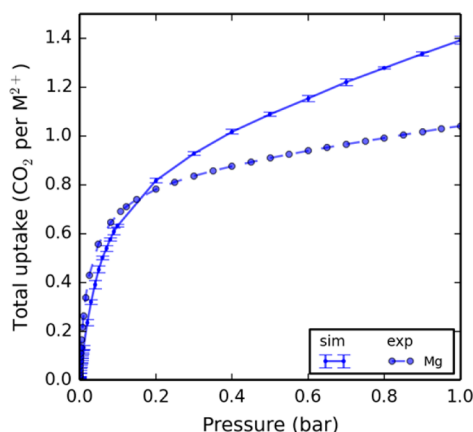


Figure 14. Comparison between the experimental and simulated isotherms computed using the DFT-derived force field for CO₂ in Mg₂(dobpdc) at 298 K. Isotherms were measured in this work for the Mg framework for comparison with simulation. The corresponding scaled isotherm from simulation is shown by the solid lines. Error bars are plotted for simulation data but in most cases smaller than the markers.

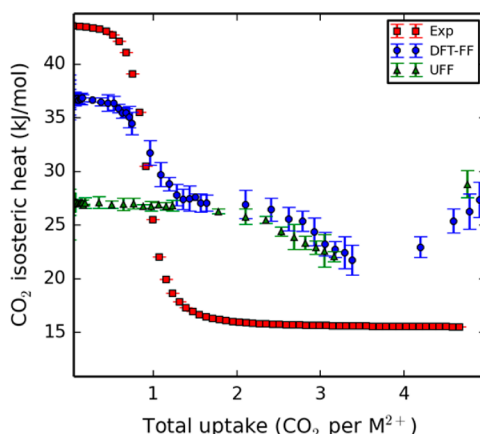


Figure 15. Comparison between the experimental (red squares) and simulated heats of adsorption as a function of the uptake computed using the DFT-derived force field (blue circles) and the UFF force field (green triangles) for CO₂ in Mg₂(dobpdc). Error bars are plotted for simulation data.

adsorption for CO₂ neither capture the triple-site behavior that is observed in simulations using the DFT-derived force field nor the increase in the heat of adsorption observed at higher uptakes (due to favorable guest–guest interactions) when using both the DFT-derived force field and the UFF force field. This is not surprising as experimentally the isosteric heats end up giving averaged out information on the many binding sites if they are not different enough in energy. Nonetheless, using the DFT-derived force field, we are able to capture the inflection point observed in the isosteric heat at an uptake of ~1 CO₂/M²⁺, which is not seen when using the UFF force field. A second inflection point in the heat of adsorption is observed at an uptake of ~2.8 CO₂/M²⁺ with both models used in simulation, followed by a gradual increase in the heat of adsorption with the increasing uptake. Additional experimentally measured CO₂ isotherms at different temperatures in Mg₂(dobpdc) are available in Figure S49.

IV.b. CH₄. Computed total CH₄ adsorption isotherms for M₂(dobpdc) frameworks using the DFT-derived force field are available in Figure S48. As in the case of CO₂, we observe adsorption behavior in the extended frameworks similar to that found in MOF-74 frameworks below 1 bar (Figure 16), but we

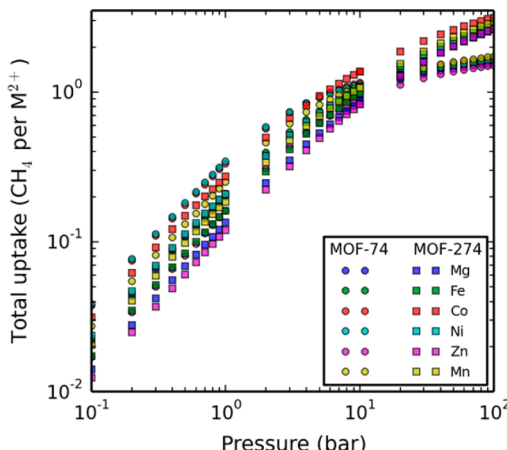


Figure 16. Comparison of CH₄ adsorption isotherms computed at 298 K using the DFT-derived force field in MOF-74 (circular markers) and M₂(dobpdc) (square markers) frameworks on a logarithmic plot.

find a higher uptake in the extended structures above this pressure due to the larger pore volume. Furthermore, similar to the case of CO₂, at low (<1 bar) pressures we actually observe slightly lower uptake in each M₂(dobpdc) framework than what was observed in the corresponding MOF-74 framework.

Simulation results for CH₄ adsorption in Mg₂(dobpdc) using the DFT-derived force field are compared to experimental measurements in Figure 17. In addition, the heats of adsorption for CH₄ in Mg₂(dobpdc) computed using the DFT-derived FF and the UFF force field are compared to experimental measurements in Figure 18. We find that not only are the computed and experimentally obtained isotherms in good agreement, but that the heats of adsorption are also in very good agreement. Although below uptakes of 0.5 CH₄ per M²⁺ the UFF force field leads to better agreement with the experimentally measured isosteric heat of adsorption, the DFT-derived force field does a better job than the UFF force field of reproducing the trend in the heat of adsorption throughout the range of CH₄ uptakes observed, and heats of adsorption computed with the DFT-derived force field are always within

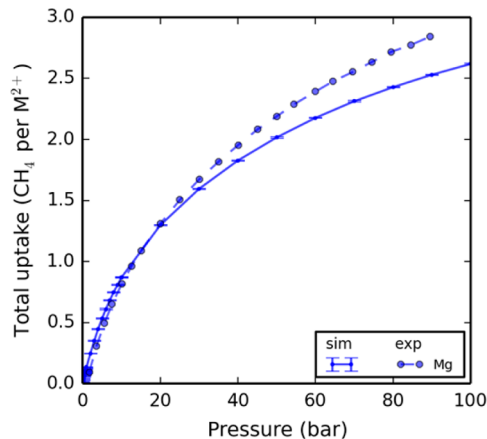


Figure 17. Comparison between the experimental and simulated isotherms computed using the DFT-derived force field for CH_4 in $\text{Mg}_2(\text{dobpdc})$ at 298 K. Isotherms were measured in this work for the Mg framework for comparison with simulation. The corresponding unscaled isotherm from simulation is shown by the solid lines. Error bars are plotted for simulation data but in most cases smaller than the markers.

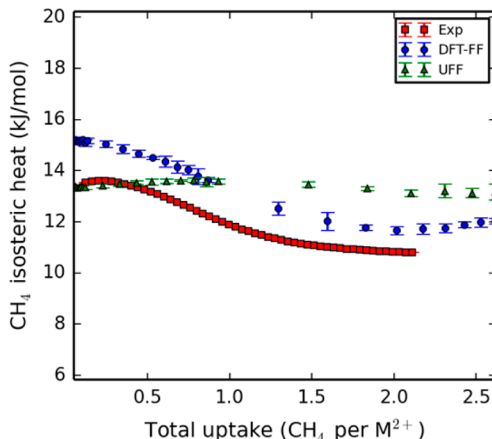


Figure 18. Comparison between the experimental (red squares) and simulated heats of adsorption as a function of the uptake computed using the DFT-derived force field (blue circles) and the UFF force field (green triangles) for CH_4 in $\text{Mg}_2(\text{dobpdc})$. Error bars are plotted for simulation data.

1.6 kJ/mol of the experimental values. As a result, we can see that the DFT-derived force field is transferable to this system for studying CH_4 adsorption across the entire range of pressures considered here. Additional experimentally measured CH_4 isotherms at different temperatures in $\text{Mg}_2(\text{dobpdc})$ are available in Figure S50.

CONCLUSION

We have developed accurate, nonpolarizable force fields for H_2O , CO_2 , and CH_4 in MOFs possessing strong-binding open-metal sites from DFT calculations. Using these force fields, we can make more accurate predictions of the adsorption properties of complex gas mixtures in M-MOF-74, including the different adsorption mechanisms and selectivities observed between the six metal frameworks studied here. From our simulations, we are able to conclude that Mg-MOF-74 would be the best of the MOF-74 frameworks for separating CO_2 from dry natural gas feeds of interest, as has also been shown by

other groups. In the case of tertiary mixtures, we find that all of the metal frameworks adsorb significantly more CO_2 than CH_4 and N_2 , with almost no N_2 adsorbed under natural gas purification conditions. We also demonstrate that lowering the temperature of the adsorption process from 313 to 287 K significantly improves the ratio of CO_2 adsorbed over the two other guests. As it has the largest CO_2 binding energy of the six frameworks studied, Mg-MOF-74 adsorbed the greatest amount of CO_2 when no H_2O was present. However, all of the studied frameworks become saturated with H_2O in the presence of $\text{CO}_2/\text{H}_2\text{O}$ binary mixtures composed of greater than 1% mole fraction of H_2O . As a result, none of these frameworks would be suitable for gas separations from any wet mixtures, especially if the mixture is composed of more weakly binding gases than CO_2 . We showed that our force field can also be used to predict adsorption behavior in other frameworks, such as the extended MOF-74 framework, $\text{M}_2(\text{dobpdc})$. Because our force field is a promising means for studying adsorption in similar frameworks, this and similar models can be used to discover new materials of similar topologies for targeted carbon capture applications and to explore the properties of existing materials. Finally, it is anticipated that the method presented here can be used to develop nonpolarizable force fields for other frameworks where existing models are not accurate enough for modeling adsorption processes of interest.

ASSOCIATED CONTENT

S Supporting Information

The Supporting Information is available free of charge on the ACS Publications website at DOI: [10.1021/acs.jpcc.6b03393](https://doi.org/10.1021/acs.jpcc.6b03393).

Definition of atom-types in the frameworks, guest-framework interaction energies along approaching paths, additional single- and multicomponent isotherms, probability density plots for all guests in the various frameworks, additional low-pressure CO_2 isotherm measurements, high-pressure CH_4 and CO_2 isotherm measurements, and dual-site Langmuir isotherm fits, force field parameters, and crystallographic data ([PDF](#))

AUTHOR INFORMATION

Corresponding Author

*Phone: +41 21 69 30079. E-mail: berend.smit@berkeley.edu.

Notes

The authors declare no competing financial interest.

ACKNOWLEDGMENTS

This material is based upon work supported as part of the Center for Gas Separations Relevant to Clean Energy Technologies, an Energy Frontier Research Center funded by the U.S. Department of Energy, Office of Science, Office of Basic Energy Sciences under award number DE-SC0001015. Work at the Molecular Foundry was supported by the Office of Science, Office of Basic Energy Sciences, of the U.S. Department of Energy under contract no. DE-AC02-05CH11231. This research used resources of the National Energy Research Scientific Computing Center, a DOE Office of Science User Facility supported by the Office of Science of the U.S. Department of Energy under Contract No. DE-AC02-05CH11231. Work at the Advanced Light Source is supported by the Director, Office of Science, Office of Basic Energy Sciences, of the U.S. Department of Energy under contract no.

DE-AC02-05CH11231. R.M. and M.T.K. acknowledge support from NSF Graduate Research Fellowships. In addition, we thank Jeffrey R. Long for helpful comments and discussions.

■ REFERENCES

- (1) Britt, D.; Furukawa, H.; Wang, B.; Glover, T. G.; Yaghi, O. M. Highly Efficient Separation of Carbon Dioxide by a Metal-Organic Framework Replete with Open Metal Sites. *Proc. Natl. Acad. Sci. U. S. A.* **2009**, *106* (49), 20637–20640.
- (2) Furukawa, H.; Cordova, K. E.; O’Keeffe, M.; Yaghi, O. M. The Chemistry and Applications of Metal-Organic Frameworks. *Science* **2013**, *341* (6149), 1230444.
- (3) D’Alessandro, D. M.; Smit, B.; Long, J. R. Carbon Dioxide Capture: Prospects for New Materials. *Angew. Chem., Int. Ed.* **2010**, *49* (35), 6058–6082.
- (4) Sumida, K.; Rogow, D. L.; Mason, J. A.; McDonald, T. M.; Bloch, E. D.; Herm, Z. R.; Bae, T.-H.; Long, J. R. Carbon Dioxide Capture in Metal-Organic Frameworks. *Chem. Rev.* **2012**, *112* (2), 724–781.
- (5) Keskin, S.; van Heest, T. M.; Sholl, D. S. Can Metal-Organic Framework Materials Play a Useful Role in Large-Scale Carbon Dioxide Separations? *ChemSusChem* **2010**, *3* (8), 879–891.
- (6) Simmons, J. M.; Wu, H.; Zhou, W.; Yildirim, T. Carbon Capture in Metal-organic Frameworks—a Comparative Study. *Energy Environ. Sci.* **2011**, *4* (6), 2177.
- (7) Rosi, N. L.; Kim, J.; Eddaoudi, M.; Chen, B.; O’Keeffe, M.; Yaghi, O. M. Rod Packings and Metal-Organic Frameworks Constructed from Rod-Shaped Secondary Building Units. *J. Am. Chem. Soc.* **2005**, *127* (5), 1504–1518.
- (8) Mason, J. A.; Sumida, K.; Herm, Z. R.; Krishna, R.; Long, J. R. Evaluating Metal-organic Frameworks for Post-Combustion Carbon Dioxide Capture via Temperature Swing Adsorption. *Energy Environ. Sci.* **2011**, *4* (8), 3030.
- (9) Yang, D.-A.; Cho, H.-Y.; Kim, J.; Yang, S.-T.; Ahn, W.-S. CO 2 Capture and Conversion Using Mg-MOF-74 Prepared by a Sonochemical Method. *Energy Environ. Sci.* **2012**, *5* (4), 6465–6473.
- (10) Caskey, S. R.; Wong-Foy, A. G.; Matzger, A. J. Dramatic Tuning of Carbon Dioxide Uptake via Metal Substitution in a Coordination Polymer with Cylindrical Pores. *J. Am. Chem. Soc.* **2008**, *130* (33), 10870–10871.
- (11) Millward, A. R.; Yaghi, O. M. Metal-Organic Frameworks with Exceptionally High Capacity for Storage of Carbon Dioxide at Room Temperature. *J. Am. Chem. Soc.* **2005**, *127* (51), 17998–17999.
- (12) Queen, W. L.; Hudson, M. R.; Bloch, E. D.; Mason, J. A.; Gonzalez, M. I.; Lee, J. S.; Gygi, D.; Howe, J. D.; Lee, K.; Darwish, T. A.; et al. Comprehensive Study of Carbon Dioxide Adsorption in the Metal-organic Frameworks M 2 (Dobdc) ($M = \text{Mg, Mn, Fe, Co, Ni, Cu, Zn}$). *Chem. Sci.* **2014**, *5* (12), 4569–4581.
- (13) Kong, X.; Scott, E.; Ding, W.; Mason, J. A.; Long, J. R.; Reimer, J. A. CO2 Dynamics in a Metal-Organic Framework with Open Metal Sites. *J. Am. Chem. Soc.* **2012**, *134* (35), 14341–14344.
- (14) Lin, L.-C.; Kim, J.; Kong, X.; Scott, E.; McDonald, T. M.; Long, J. R.; Reimer, J. A.; Smit, B. Understanding CO 2 Dynamics in Metal-Organic Frameworks with Open Metal Sites. *Angew. Chem.* **2013**, *125* (16), 4506–4509.
- (15) Poloni, R.; Lee, K.; Berger, R. F.; Smit, B.; Neaton, J. B. Understanding Trends in CO2 Adsorption in Metal-Organic Frameworks with Open-Metal Sites. *J. Phys. Chem. Lett.* **2014**, *5* (5), 861–865.
- (16) Lee, K.; Howe, J. D.; Lin, L.-C.; Smit, B.; Neaton, J. B. Small-Molecule Adsorption in Open-Site Metal-Organic Frameworks: A Systematic Density Functional Theory Study for Rational Design. *Chem. Mater.* **2015**, *27* (3), 668–678.
- (17) Lin, L.-C.; Berger, A. H.; Martin, R. L.; Kim, J.; Swisher, J. A.; Jariwala, K.; Rycroft, C. H.; Bhown, A. S.; Deem, M. W.; Haranczyk, M.; et al. In Silico Screening of Carbon-Capture Materials. *Nat. Mater.* **2012**, *11* (7), 633–641.
- (18) Kim, J.; Abouelnasr, M.; Lin, L.-C.; Smit, B. Large-Scale Screening of Zeolite Structures for CO2 Membrane Separations. *J. Am. Chem. Soc.* **2013**, *135* (20), 7545–7552.
- (19) Krishna, R.; van Baten, J. M. In Silico Screening of Metal-Organic Frameworks in Separation Applications. *Phys. Chem. Chem. Phys.* **2011**, *13* (22), 10593–10616.
- (20) Krishna, R.; van Baten, J. M. In Silico Screening of Zeolite Membranes for CO2 Capture. *J. Membr. Sci.* **2010**, *360* (1–2), 323–333.
- (21) Rappe, A. K.; Casewit, C. J.; Colwell, K. S.; Goddard, W. A.; Skiff, W. M. UFF, a Full Periodic Table Force Field for Molecular Mechanics and Molecular Dynamics Simulations. *J. Am. Chem. Soc.* **1992**, *114* (25), 10024–10035.
- (22) Mayo, S. L.; Olafson, B. D.; Goddard, W. A. DREIDING: A Generic Force Field for Molecular Simulations. *J. Phys. Chem.* **1990**, *94* (26), 8897–8909.
- (23) Simon, C. M.; Kim, J.; Gomez-Gualdrón, D. A.; Camp, J. S.; Chung, Y. G.; Martin, R. L.; Mercado, R.; Deem, M. W.; Gunter, D.; Haranczyk, M.; et al. The Materials Genome in Action: Identifying the Performance Limits for Methane Storage. *Energy Environ. Sci.* **2015**, *8* (4), 1190–1199.
- (24) Chen, L.; Morrison, C. A.; Düren, T. Improving Predictions of Gas Adsorption in Metal-Organic Frameworks with Coordinatively Unsaturated Metal Sites: Model Potentials, Ab Initio Parameterization, and GCMC Simulations. *J. Phys. Chem. C* **2012**, *116* (35), 18899–18909.
- (25) Fang, H.; Kamakoti, P.; Zang, J.; Cundy, S.; Paur, C.; Ravikovich, P. I.; Sholl, D. S. Prediction of CO 2 Adsorption Properties in Zeolites Using Force Fields Derived from Periodic Dispersion-Corrected DFT Calculations. *J. Phys. Chem. C* **2012**, *116* (19), 10692–10701.
- (26) Haldoupis, E.; Borycz, J.; Shi, H.; Vogiatzis, K. D.; Bai, P.; Queen, W. L.; Gagliardi, L.; Siepmann, J. I. Ab Initio Derived Force Fields for Predicting CO 2 Adsorption and Accessibility of Metal Sites in the Metal-Organic Frameworks M-MOF-74 ($M = \text{Mn, Co, Ni, Cu}$). *J. Phys. Chem. C* **2015**, *119* (28), 16058–16071.
- (27) Borycz, J.; Lin, L.-C.; Bloch, E. D.; Kim, J.; Dzubak, A. L.; Maurice, R.; Semrouni, D.; Lee, K.; Smit, B.; Gagliardi, L. CO 2 Adsorption in Fe 2 (Dobdc): A Classical Force Field Parameterized from Quantum Mechanical Calculations. *J. Phys. Chem. C* **2014**, *118* (23), 12230–12240.
- (28) Dzubak, A. L.; Lin, L.-C.; Kim, J.; Swisher, J. A.; Poloni, R.; Maximoff, S. N.; Smit, B.; Gagliardi, L. Ab Initio Carbon Capture in Open-Site Metal-Organic Frameworks. *Nat. Chem.* **2012**, *4* (10), 810–816.
- (29) Lin, L.-C.; Lee, K.; Gagliardi, L.; Neaton, J. B.; Smit, B. Force-Field Development from Electronic Structure Calculations with Periodic Boundary Conditions: Applications to Gaseous Adsorption and Transport in Metal-Organic Frameworks. *J. Chem. Theory Comput.* **2014**, *10* (4), 1477–1488.
- (30) Mason, J. A.; McDonald, T. M.; Bae, T.-H.; Bachman, J. E.; Sumida, K.; Dutton, J. J.; Kaye, S. S.; Long, J. R. Application of a High-Throughput Analyzer in Evaluating Solid Adsorbents for Post-Combustion Carbon Capture via Multicomponent Adsorption of CO2, N2, and H2O. *J. Am. Chem. Soc.* **2015**, *137* (14), 4787–4803.
- (31) Harris, J. G.; Yung, K. H. Carbon Dioxide’s Liquid-Vapor Coexistence Curve And Critical Properties as Predicted by a Simple Molecular Model. *J. Phys. Chem.* **1995**, *99* (31), 12021–12024.
- (32) Martin, M. G.; Siepmann, J. I. Transferable Potentials for Phase Equilibria. 1. United-Atom Description of N-Alkanes. *J. Phys. Chem. B* **1998**, *102* (14), 2569–2577.
- (33) Horn, H. W.; Swope, W. C.; Pitera, J. W.; Madura, J. D.; Dick, T. J.; Hura, G. L.; Head-Gordon, T. Development of an Improved Four-Site Water Model for Biomolecular Simulations: TIP4P-Ew. *J. Chem. Phys.* **2004**, *120* (20), 9665–9678.
- (34) Horn, H. W.; Swope, W. C.; Pitera, J. W. Characterization of the TIP4P-Ew Water Model: Vapor Pressure and Boiling Point. *J. Chem. Phys.* **2005**, *123* (19), 194504.

- (35) Kresse, G. Efficient Iterative Schemes for Ab Initio Total-Energy Calculations Using a Plane-Wave Basis Set. *Phys. Rev. B: Condens. Matter Mater. Phys.* **1996**, *54* (16), 11169–11186.
- (36) Perdew, J. P.; Burke, K.; Ernzerhof, M. Generalized Gradient Approximation Made Simple. *Phys. Rev. Lett.* **1996**, *77* (18), 3865–3868.
- (37) Lee, K.; Murray, É. D.; Kong, L.; Lundqvist, B. I.; Langreth, D. C. Higher-Accuracy van Der Waals Density Functional. *Phys. Rev. B: Condens. Matter Mater. Phys.* **2010**, *82* (8), 081101.
- (38) Kresse, G. From Ultrasoft Pseudopotentials to the Projector Augmented-Wave Method. *Phys. Rev. B: Condens. Matter Mater. Phys.* **1999**, *59* (3), 1758–1775.
- (39) Blöchl, P. E. Projector Augmented-Wave Method. *Phys. Rev. B: Condens. Matter Mater. Phys.* **1994**, *50* (24), 17953–17979.
- (40) Wang, L.; Maxisch, T.; Ceder, G. Oxidation Energies of Transition Metal Oxides within the GGA + U Framework. *Phys. Rev. B: Condens. Matter Mater. Phys.* **2006**, *73* (19), 195107.
- (41) Campañá, C.; Mussard, B.; Woo, T. K. Electrostatic Potential Derived Atomic Charges for Periodic Systems Using a Modified Error Functional. *J. Chem. Theory Comput.* **2009**, *5* (10), 2866–2878.
- (42) Grimme, S. Semiempirical GGA-Type Density Functional Constructed with a Long-Range Dispersion Correction. *J. Comput. Chem.* **2006**, *27* (15), 1787–1799.
- (43) Geier, S. J.; Mason, J. A.; Bloch, E. D.; Queen, W. L.; Hudson, M. R.; Brown, C. M.; Long, J. R. Selective Adsorption of Ethylene over Ethane and Propylene over Propane in the Metal–organic Frameworks M2(dobdc) (M = Mg, Mn, Fe, Co, Ni, Zn). *Chem. Sci.* **2013**, *4* (5), 2054.
- (44) Sanz, R.; Martínez, F.; Orcajo, G.; Wojtas, L.; Briones, D. Synthesis of a Honeycomb-like Cu-Based Metal–organic Framework and Its Carbon Dioxide Adsorption Behaviour. *Dalt. Trans.* **2013**, *42* (7), 2392–2398.
- (45) McDonald, T. M.; Mason, J. A.; Kong, X.; Bloch, E. D.; Gygi, D.; Dani, A.; Crocellà, V.; Giordanino, F.; Odoh, S. O.; Drisdell, W. S.; et al. Cooperative Insertion of CO₂ in Diamine-Appended Metal–Organic Frameworks. *Nature* **2015**, *519* (7543), 303–308.
- (46) Mason, J. A.; Veenstra, M.; Long, J. R. Evaluating Metal–Organic Frameworks for Natural Gas Storage. *Chem. Sci.* **2014**, *5* (1), 32–51.
- (47) Lemmon, E. W.; Huber, M. L.; McLinden, M. O. *NIST Standard Reference Database 23. Ref. Fluid Thermodyn. Transp. Prop.*, 2012.
- (48) Martin, M. G.; Siepmann, J. I. Transferable Potentials for Phase Equilibria. 1. United-Atom Description of N-Alkanes. *J. Phys. Chem. B* **1998**, *102*, 2569–2577.
- (49) Surblé, S.; Millange, F.; Serre, C.; Düren, T.; Latroche, M.; Bourrelly, S.; Llewellyn, P. L.; Férey, G. Synthesis of MIL-102, a Chromium Carboxylate Metal–Organic Framework, with Gas Sorption Analysis. *J. Am. Chem. Soc.* **2006**, *128* (46), 14889–14896.
- (50) Dubbeldam, D.; Frost, H.; Walton, K. S.; Snurr, R. Q. Molecular Simulation of Adsorption Sites of Light Gases in the Metal–Organic Framework IRMOF-1. *Fluid Phase Equilib.* **2007**, *261* (1–2), 152–161.
- (51) Demir, H.; Greathouse, J. A.; Staiger, C. L.; Perry, J. J., IV; Allendorf, M. D.; Sholl, D. S. DFT-Based Force Field Development for Noble Gas Adsorption in Metal Organic Frameworks. *J. Mater. Chem. A* **2015**, *3*, 23539–23548.
- (52) Childs, H.; Brugger, E.; Whitlock, B.; Meredith, J.; Ahern, S.; Pugmire, D.; Biagas, K.; Miller, M.; Harrison, C.; Weber, G. H.; et al. VisIt: An End-User Tool For Visualizing and Analyzing Very Large Data. *High Performance Visualization—Enabling Extreme-Scale Scientific Insight* **2012**, *20124456*, 357–372.
- (53) Schoenecker, P. M.; Carson, C. G.; Jasuja, H.; Flemming, C. J. J.; Walton, K. S. Effect of Water Adsorption on Retention of Structure and Surface Area of Metal–Organic Frameworks. *Ind. Eng. Chem. Res.* **2012**, *51* (18), 6513–6519.
- (54) Glover, T. G.; Peterson, G. W.; Schindler, B. J.; Britt, D.; Yaghi, O. MOF-74 Building Unit Has a Direct Impact on Toxic Gas Adsorption. *Chem. Eng. Sci.* **2011**, *66* (2), 163–170.
- (55) Mark, P.; Nilsson, L. Structure and Dynamics of the TIP3P, SPC, and SPC/E Water Models at 298 K. *J. Phys. Chem. A* **2001**, *105* (43), 9954–9960.
- (56) Jorgensen, W. L.; Chandrasekhar, J.; Madura, J. D.; Impey, R. W.; Klein, M. L. Comparison of Simple Potential Functions for Simulating Liquid Water. *J. Chem. Phys.* **1983**, *79* (2), 926.
- (57) Vega, C.; Sanz, E.; Abascal, J. L. F. The Melting Temperature of the Most Common Models of Water. *J. Chem. Phys.* **2005**, *122* (11), 114507.
- (58) Castillo, J. M.; Dubbeldam, D.; Vlugt, T. J. H.; Smit, B.; Calero, S. Evaluation of Various Water Models for Simulation of Adsorption in Hydrophobic Zeolites. *Mol. Simul.* **2009**, *35* (12–13), 1067–1076.
- (59) Mao, Y.; Zhang, Y. Prediction of the Temperature-Dependent Thermal Conductivity and Shear Viscosity for Rigid Water Models. *J. Nanotechnol. Eng. Med.* **2012**, *3* (3), 031009.
- (60) Mahoney, M. W.; Jorgensen, W. L. A Five-Site Model for Liquid Water and the Reproduction of the Density Anomaly by Rigid, Nonpolarizable Potential Functions. *J. Chem. Phys.* **2000**, *112* (20), 8910.
- (61) Rick, S. W. A Reoptimization of the Five-Site Water Potential (TIPSP) for Use with Ewald Sums. *J. Chem. Phys.* **2004**, *120* (13), 6085–6093.
- (62) Nada, H.; van der Eerden, J. P. J. M. An Intermolecular Potential Model for the Simulation of Ice and Water near the Melting Point: A Six-Site Model of H₂O. *J. Chem. Phys.* **2003**, *118* (16), 7401.
- (63) Rudenko, A. N.; Bendt, S.; Keil, F. J. Multiscale Modeling of Water in Mg-MOF-74: From Electronic Structure Calculations to Adsorption Isotherms. *J. Phys. Chem. C* **2014**, *118* (29), 16218–16227.
- (64) Peng, X.; Lin, L.-C.; Sun, W.; Smit, B. Water Adsorption in Metal–Organic Frameworks with Open-Metal Sites. *AIChE J.* **2015**, *61* (2), 677–687.
- (65) Grande, C. A.; Blom, R. *Energy Procedia* **2012**, *26* (1876), 2–14.
- (66) Rappe, A. K.; Goddard, W. A. Charge Equilibration for Molecular Dynamics Simulations. *J. Phys. Chem.* **1991**, *95* (8), 3358–3363.
- (67) O’Boyle, N. M.; Banck, M.; James, C. A.; Morley, C.; Vandermeersch, T.; Hutchison, G. R. Open Babel: An Open Chemical Toolbox. *J. Cheminf.* **2011**, *3* (1), 33.